photonics

MDPI

Article

Zoom Long-Wave Infrared Constant Ground Resolution Imaging Optical System Design

Zhiqiang Yang, Wenna Zhang, Bohan Wu, Liguo Wang, Yao Li, Lihong Yang and Lei Gong *

School of Opto-Electronic Engineering, Xi'an Technology University, Xi'an 710021, China; yangzhiqiang@xatu.edu.cn (Z.Y.); zhangwenna@st.xatu.edu.cn (W.Z.); wubohan@st.xatu.edu.cn (B.W.); wangliguo@xatu.edu.cn (L.W.); liyao@xatu.edu.cn (Y.L.); yanglihong@xatu.edu.cn (L.Y.)
* Correspondence: gonglei@xatu.edu.cn

Abstract

Long-wave infrared (LWIR) airborne optical systems for ground imaging are widely utilized in applications such as ground reconnaissance, agricultural monitoring, counterterrorism, and other fields. Traditional oblique-view ground-imaging optical systems suffer from a critical drawback compared to nadir-view systems: the significant variation in object distances between distant and nearby targets. This disparity leads to inconsistent ground resolution (GR), manifesting in images where distant targets exhibit significantly lower resolution than nearby ones. This characteristic is highly detrimental to information acquisition and three-dimensional modeling of the system. Furthermore, the limited field of view of fixed focal length systems prevents the unmanned aerial vehicle (UAV) from acquiring target information effectively across varying flight altitudes. To address this issue, this paper designs an oblique imaging optical system capable of achieving both constant GR and zoom functionality in the LWIR band. By controlling the ground resolution, a LWIR continuous zoom optical system was designed. The system maintains constant GR over the entire field of view. Its modulation transfer function (MTF) approaches the diffraction limit across the full field of view, and the spot diagram remains within Airy's disk at each view angle. The radius of the spot diagram is smaller than that of the Airy disk, indicating that the geometric aberrations of the system are well corrected. The imaging performance is primarily determined by the wavelength and the F-number. In the case of LWIR, the longer wavelength results in a larger Airy disk radius. The system meets imaging quality requirements and is suitable for air-to-ground target reconnaissance imaging.

Keywords: catadioptric optical system; constant ground resolution; free-form surfaces; zoom optical system; field-of-view focal length

Check for updates

Received: 27 January 2026
Revised: 7 March 2026
Accepted: 25 March 2026
Published: 29 March 2026

Copyright: © 2026 by the authors. Licensee MDPI, Basel, Switzerland. This article is an open access article distributed under the terms and conditions of the Creative Commons Attribution (CC BY) license.

1. Introduction

Airborne electro-optical detection systems, as a critical component of aerial reconnaissance architectures, leverage their unique technological advantages to achieve a paradigm shift from intelligence gathering to decision support. In particular, electro-optical pods operating in the long-wave infrared band perform detection and reconnaissance passively—without emitting signals—thereby offering superior covertness. These systems enable continuous surveillance and precise identification of distant targets across various weather conditions. In military applications, these systems significantly enhance the situational awareness, velocity and intelligence processing efficiency of combat units, serving as a

critical technological enabler for seizing battlefield initiative [1,2]. Furthermore, its applications in border surveillance, drone detection, and gas leak detection are also becoming increasingly widespread [3].

Oblique-view cameras can be mounted on unmanned aerial vehicles (UAVs) and aircraft to provide multi-perspective surveillance imagery, effectively covering areas that are inaccessible to traditional nadir-view detection. The oblique angle is particularly well-suited for complex terrains and provides significant assistance for post-processing tasks such as 3D reconstruction [4]. Moreover, in specific terrains like border areas, it aids border patrol officers in detecting illegal crossings by both personnel and animals. Similarly, oblique-view cameras can also be widely applied in remote sensing and geographic information systems, aeronautics and astronautics, and agricultural monitoring.

In 2019, Zhu J et al. proposed the concept of field-of-view focal length (FFL) and employed a point-by-point iterative construction method to design an airborne oblique imaging optical system for visible light. This system achieved uniform ground resolution [5]. In the same year, Wu W et al. proposed a field-expansion construction method to develop a low-F-number, $40^\circ \times 30^\circ$ wide rectangular field-of-view free-form surface far-infrared camera. This design optimizes imaging near the diffraction limit, with a prototype validated to achieve high image quality [6]. In 2021, Wu W et al. proposed a direct design method based on field-of-view-related parameters to construct a three-degree-of-freedom curved off-axis system with high central and low peripheral resolution characteristics, achieving high-quality imaging across a $30^\circ \times 30^\circ$ square field of view [7]. In the same year, Haiqing W et al. proposed a $22\times$ dual-mode miniaturized infrared continuous zoom system featuring a non-focal front group and an extended focal rear group. Switching between long and short focal lengths meets the long-range and close-range detection requirements of airborne pods, with imaging quality approaching the diffraction limit [8]. In 2024, Cheng Y et al. proposed a lightweight, low-cost, uncooled long-wave infrared continuous zoom system driven by a dielectric elastomer-actuated Alvarez lens, achieving $5\times$ to $15\times$ zoom without mechanical movement [9]. In 2025, LIU H et al. proposed a passive non-line-of-sight imaging technique based on the deep fusion of KAN networks across three spectral bands—visible to long-wave infrared—enabling real-time, high-quality reconstruction of distant covert targets [10].

There are two limitations in the existing constant ground resolution imaging technology: first, research has predominantly focused on the visible or mid-wave infrared (MWIR) bands, while studies on long-wave infrared (LWIR) terrestrial constant ground resolution systems remain scarce; second, existing designs are mostly fixed-focus, and the constant ground resolution control under continuous zoom conditions remains unresolved. Furthermore, engineering implementation literature regarding LWIR zoom systems in recent years is relatively scarce, reflecting that this field is still in its developmental stages. This paper and literature [11] are the work of the same research team, but there is a clear division of labor: literature [11] focuses on the MWIR fixed-focus system, whereas this paper focuses on the LWIR zoom system. The two studies differ in terms of wave bands and design objectives, so there is no duplication.

In response to the aforementioned limitations, this paper addresses the issues of non-uniform resolution and poor adaptability to fixed focal lengths in traditional LWIR airborne oblique imaging systems by designing an optical system that integrates constant ground resolution with zoom functionality. The main innovations are as follows:

(1) Applying freeform surface XY polynomials to achieve constant ground resolution imaging in the LWIR band.
(2) Achieving a continuous zoom range from 50 mm to 100 mm while maintaining uniform ground resolution across the zoom range.

(3) Adopting a catadioptric structure combining an off-axis three-mirror system with a relay zoom group, reducing ground resolution deviation to 0.004 m within the flight altitude range of 1.6 km to 3.3 km.

2. System Calculation

2.1. System Operational Parameter Calculation

According to the requirements of the airborne optical system, the UAV operates at an altitude of 1.6 to 3.3 km for target identification, based on the Johnson criteria:

$$\frac{R}{H} = \frac{f'}{N \times a} \tag{1}$$

R is the detection and identification distance of the optical system for a target; H is the operational altitude; f' is the detection and identification focal length of the optical system; N is the number of pixels for detecting and identifying the target (the number of pixels can be selected according to the Johnson criteria); a is the pixel size of the detector [12]. A LWIR detector with a pixel resolution of 640 × 512 and a pixel size of 15 μm was selected. With N set to 4, the calculated focal length variation range is 50–100 mm.

The Nyquist frequency N_n of the system transfer function is:

$$N_n = \frac{1}{2a} \approx 33.3 \text{ lp/mm} \tag{2}$$

The system performance parameters are listed in Table 1.

Table 1. System Performance Parameters.

Parameters	Numerical Value
Operating bands	8–12 μm
Focal length	50–100 mm
Rectangular field of view	10.86° × 8.78°–5.5° × 4.4°
Detector pixel resolution	640 × 512
Pixel size	15 μm

2.2. Calculation of the Relationship Between Field-of-View Focal Length and Ground Resolution

We analyze the imaging characteristics of an optical system when the object is located at a distant position (approximately at infinity) [11]. The field of view is ω. Chief rays near the field of view ω focus on a point on the image plane, while chief rays from an adjacent field of view $\boldsymbol{\omega}'$ focus on another point on the image plane (where $\boldsymbol{\omega}'$ is obtained by introducing a small field angle increment $\Delta\omega$ into the ω field). The spatial distance between these two image points is Δh, $FFL(\omega)$ is referred to as the field-of-view focal length, which is defined as the ratio of the tangent of the Δh to that of the $\Delta\omega$, i.e.,:

$$FFL(\omega) = \frac{\Delta h}{\tan(\Delta\omega)} \approx \frac{\Delta h}{\Delta\omega} \tag{3}$$

The schematic diagram of the relationship between ground resolution and instantaneous field of view is shown in Figure 1.

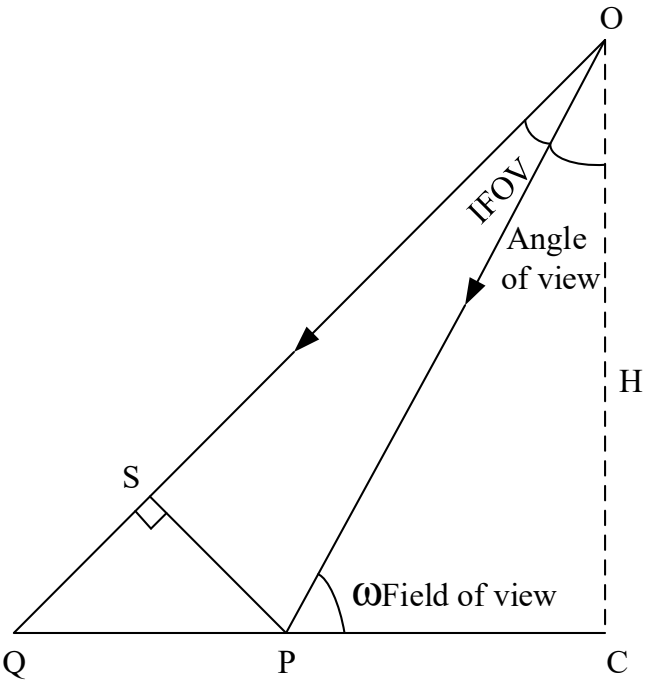


Figure 1. Schematic diagram of the relationship between ground resolution and instantaneous field of view.

For the convenience of calculation, an approximate approach is adopted here to derive the relationship between the ground resolution and the field-of-view focal length (FFL) [13]. Given that $\angle POQ$ is very small, it follows that $\angle COP \approx \angle COQ$ and $\angle CPO \approx \angle CQO$, leading to $\angle QPS \approx \angle COP$. Therefore:

$$PS = PQ \times cos(\angle QPS) \approx PQ \times cos(\angle COP) \tag{4}$$

Since the instantaneous field of view angle is very small and PQ is also very small, OP and OS are approximately equal. Therefore:

$$tan(\angle POQ) = \frac{PS}{OS} \approx \frac{PS}{OP} \approx \frac{PQ \times cos(\angle COP)}{OP} \approx \frac{PQ \times cos(\angle COP)}{H/cos(\angle COP)} \tag{5}$$

The relationship between the instantaneous field of view angle $\angle POQ$ and the field-of-view focal length is given by:

$$tan(\angle POQ) = \frac{a}{FFL(\omega)} \tag{6}$$

where a is the size of a single pixel unit. Substituting PQ with $\boldsymbol{GR}(\boldsymbol{\omega})$ and combining Equations (3)–(6), the relationship between the field-of-view focal length and the ground resolution is calculated as follows:

$$FFL(\omega) = \frac{a \times H}{GR(\omega) \times cos^2(-26^\circ + \omega)} \tag{7}$$

After obtaining the above formula, given equal values of ground resolution, individual pixel cell size, and camera altitude, the desired distribution of field-of-view focal lengths, i.e., in the formula [14], can be obtained. By setting the GR under each field of view to a uniform value, the distribution law of the desired field-of-view focal lengths for field of view angles ranging from 10° to 16° can be calculated, as shown in Figure 2.

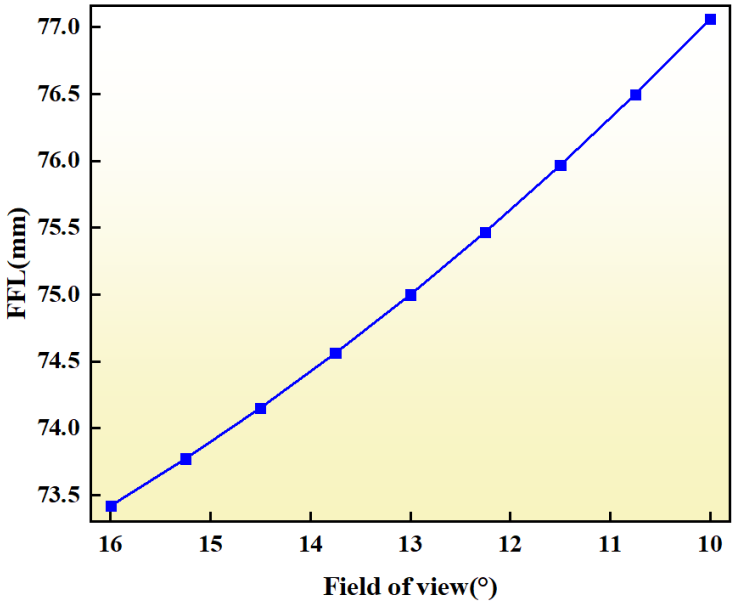


Figure 2. Distribution of the desired field-of-view focal length (FFL).

Given the distribution of the field-of-view focal lengths, i.e., $FFL(\omega)$, corresponding to each field of view, the expected image heights of each field of view can be calculated based on this distribution. The expected image heights are the new object-image relationship.

For different fields of view, light rays converge to different image points. The formula for calculating the perfect image point is as follows:

$$T = \begin{bmatrix} T_{ideal,x} \\ T_{ideal,y} \\ T_{ideal,z} \end{bmatrix} = \begin{bmatrix} 0 & 0 & 0 \\ 0 & \cos\alpha_0 & \sin\alpha_0 \\ 0 & -\sin\alpha_0 & \cos\alpha_0 \end{bmatrix} \begin{bmatrix} f\tan(\omega_x - \omega_{x,central}) \\ f\tan\left(\omega_y - \omega_{y,central}\right) \\ 0 \end{bmatrix} + \begin{bmatrix} x_0 \\ y_0 \\ z_0 \end{bmatrix} \quad (8)$$

According to Equation (8), the perfect image point for each field of view can be obtained. In the equation, α_0 is the tilt angle of the image plane with the X-axis, and (x_0, y_0, z_0) is the coordinate of the center point of the image plane.

3. Off-Axis Reflection System Design

The front-end optics of this system employ an off-axis three-mirror structure, chosen based on the following considerations: First, the off-axis design eliminates central obscuration, offers high energy utilization efficiency, which is suitable for LWIR detection with high sensitivity requirements. Second, reflective systems are free from chromatic aberration, maintaining good image quality across the wide 8–12 μm band. Third, the off-axis configuration offers significant potential for field-of-view expansion, meeting the 10–16° oblique imaging field-of-view requirements. Finally, the off-axis structure facilitates the integration of freeform surfaces, effectively correcting asymmetric aberrations and enabling the design of constant ground resolution.

In addition, the optical design, optimization and image quality analysis of this system were primarily performed in Ansys Zemax OpticStudio 2024 R1.00, and some design results are cross-verified by Code V 2024.03.

3.1. Calculation and Design Results of the Coaxial Three-Mirror Initial Structure

According to the design method of off-axis reflective systems, obtaining an off-axis structure first requires determining the coaxial reflective initial configuration.

There are two common methods to calculate the initial structural parameters of a coaxial three-mirror system: determination based on the obscuration ratio coefficient and determination based on the mirror spacing [15,16].

The initial structure of the three-mirror system is shown in Figure 3. Suppose K_1, K_2 and K_3 are the quadratic surface coefficients of the primary, secondary, and tertiary mirrors, respectively; α_1 and α_2 are the obscuration coefficients of the secondary mirror, relative to the primary mirror and the tertiary mirror relative to the secondary mirror, respectively; h_1, h_2 and h_3 are the apertures of the three mirrors; β_1 and β_2 are the magnifications of the secondary and tertiary mirrors, respectively. For the reflective system, $n_1 = n_2' = n_3 = 1$, $n_2' = n_2 = n_3' = -1$.

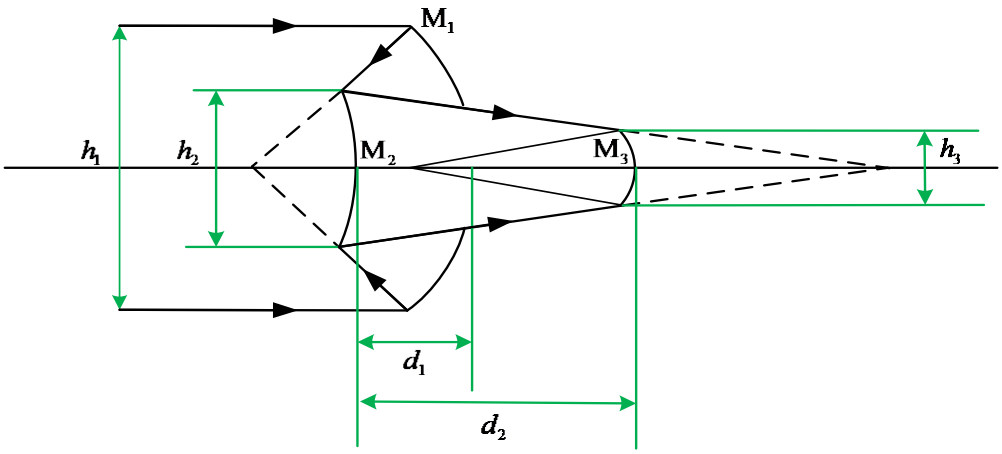


Figure 3. Schematic of the coaxial three-mirror initial structure.

(1) Determination of the three-mirror optical parameters based on the obscuration ratio.

The obscuration ratio of the secondary mirror to the primary mirror is:

$$\alpha_1 = \frac{l_2}{f_1'} \approx \frac{h_2}{h_1} \tag{9}$$

The obscuration ratio of the tertiary mirror to the secondary mirror is:

$$\alpha_2 = \frac{l_3}{l_2'} \approx \frac{h_3}{h_2} \tag{10}$$

The magnification of the secondary mirror is:

$$\beta_1 = \frac{l_2'}{l_2} = \frac{u_2}{u_2'} \tag{11}$$

The magnification of the tertiary mirror is:

$$\beta_2 = \frac{l_3'}{l_3} = \frac{u_3}{u_3'} \tag{12}$$

Based on Gaussian optics theory, the structural parameters of the system can be expressed in terms of the geometric relationships α_1, α_2, β_1 and β_2 in the above figure, as follows:

$$R_1 = \frac{2}{\beta_1\beta_2} f' \tag{13}$$

$$R_2 = \frac{2\alpha_1}{(1+\beta_1)\beta_2} f' \tag{14}$$

$$R_3 = \frac{2\alpha_1\alpha_2}{1+\beta_2} f' \tag{15}$$

d_1 is the distance from the primary mirror to the secondary mirror, d_2 is the distance from the secondary mirror to the tertiary mirror, and $L_3{}'$ is the back intercept. Among these, $d_1 < 0$, $d_2 > 0$ and $L_3{}' < 0$. Here y is the height at which the chief ray intersects each mirror surface.

$$d_1 = \frac{1-\alpha_1}{\beta_1\beta_2} f' \tag{16}$$

$$d_2 = \frac{\alpha_1(1-\alpha_2)}{\beta_2} f' \tag{17}$$

$$L_3{}' = \alpha_1\alpha_2 f' \tag{18}$$

When the aperture stop is placed at the secondary mirror:

$$y_1 = \frac{(1-\alpha_1)}{\alpha_1\beta_1\beta_2} \tag{19}$$

$$y_2 = 0 \tag{20}$$

$$y_3 = \frac{(1-\alpha_2)}{\beta_2} \tag{21}$$

There are five types of monochromatic aberrations: spherical aberration, coma, astigmatism, field curvature and distortion, with their third-order aberration coefficients being S_{I}, S_{II}, S_{III}, S_{IV} and S_{V}, respectively. In analyzing the aberrations of coaxial three-mirror optical systems, the primary focus is on spherical aberration, coma, astigmatism, and field curvature. When expressed in terms of Seidel aberrations, they are given as follows:

$$\begin{aligned} S_{\mathrm{I}} = {} & \tfrac{(k_1-1)\beta_1^3\beta_2^3}{4} - \tfrac{k_2\alpha_1\beta_2^3(1+\beta_1)^3}{4} + \tfrac{k_3\alpha_1\alpha_2(1+\beta_2)^3}{4} \\ & - \tfrac{\alpha_1\beta_2^3(1+\beta_1)(1-\beta_1)}{4} - \tfrac{\alpha_1\alpha_2(1+\beta_2)(1-\beta_2)^2}{4} \end{aligned} \tag{22}$$

$$\begin{aligned} S_{\mathrm{II}} = {} & -\tfrac{k_2(\alpha_1-1)\beta_2^3(1+\beta_1)^3}{4\beta_1\beta_2} + k_3\tfrac{[\alpha_2(\alpha_1-1)+\beta_1(1+\alpha_2)](1+\beta_2)^3}{4\beta_1\beta_2} + \\ & \tfrac{(\alpha_1-1)\beta_2^3(1+\beta_1)](1-\beta_1)^2}{4\beta_1\beta_2} - \tfrac{[\alpha_2(\alpha_1-1)+\beta_1(1-\alpha_2)](1-\beta_2)^2(1+\beta_2)}{4\beta_1\beta_2} \end{aligned} \tag{23}$$

$$\begin{aligned} S_{\mathrm{III}} = {} & -k_2\tfrac{(\alpha_1-1)^2(1-\beta_1)^3}{4\alpha_1\beta_1^2} + k_3\tfrac{[\alpha_2(\alpha_1-1)+\beta_1(1-\alpha_2)]^2(1+\beta_2)^3}{4\beta_1\beta_2\beta_1^2\beta_2^2} \\ & + \tfrac{\beta_2(\alpha_1-1)^2(1+\beta_1)(1-\beta_1)^2}{4\alpha_1\beta_1^2} - \tfrac{[\alpha_2(\alpha_1-1)+\beta_1(1-\alpha_2)]^2(1-\beta_2)^2(1+\beta_2)}{4\alpha_1\alpha_2\beta_1^2\beta_2^2} \\ & - \tfrac{\beta_2(\alpha_1-1)(1-\beta_1)(1-\beta_1)}{\alpha_1\beta_2} - \tfrac{[\alpha_2(\alpha_1-1)+\beta_1(1-\alpha_2)](1+\beta_2)(1-\beta_2)}{4\alpha_1\alpha_2\beta_1\beta_2} \\ & -\beta_1\beta_2 + \tfrac{\beta_2(1+\beta_1)}{\alpha_1} - \tfrac{(1+\beta_2)}{\alpha_1\alpha_2} \end{aligned} \tag{24}$$

$$S_{\mathrm{IV}} = \beta_1\beta_2 - \frac{\beta_2(1+\beta_1)}{\alpha_1} + \frac{(1+\beta_2)}{\alpha_1\alpha_2} \tag{25}$$

Typically, the detector used is planar, necessitating that the optical system satisfy the flat image field condition, that is $S_{\mathrm{IV}} = 0$. If three contour parameters are specified, the fourth can be derived from the flat field condition using the following formula. Let $S_{\mathrm{I}} = S_{\mathrm{II}} = S_{\mathrm{III}} = 0$, i.e., under the condition that spherical aberration, coma, and astigmatism are zero, $-e_1^2$, $-e_2^2$, and $-e_3^2$ (which have an inverse relationship to K) can be obtained from the formula. Consequently, all eight structural parameters that determine the initial configuration of the coaxial three-mirror system can be derived, allowing for the calculation of the initial structure of the optical system.

(2) Determination of the initial structure based on the mirror separation.

Combining Equations (9)–(18) gives:

$$\beta_1 = \frac{1-\alpha_1}{d_1\beta_2} f' \tag{26}$$

$$\beta_2 = \frac{\alpha_1(1-\alpha_1)}{d_2} f' \tag{27}$$

$$\alpha_2 = \frac{l_3'}{\alpha_1 f'} \tag{28}$$

Substituting Equation (28) into Equation (25) yields a quadratic equation in α_1.

$$A{\alpha_1}^2 + B\alpha_1 + c = 0 \tag{29}$$

$$\begin{cases} A = \frac{d_2 l_3'}{f'^2} - \frac{d_1}{f'} \\ B = 2\frac{l_3'}{f'^2}(d_1 - d_2) + \frac{d_1 d_2}{f'^2}. \\ C = \frac{l_3'}{f'}(\frac{d_2}{f'} - \frac{d_1 l_3'}{f'^2}) \end{cases} \tag{30}$$

Considering that the obscuration ratio is positive, then

$$\alpha_1 = \frac{-B + \sqrt{B^2 - 4AC}}{2A} \tag{31}$$

Based on Equations (26)–(28), α_2, β_1, and β_2 are solved, and then derive the aspheric coefficients $-e_1^2$, $-e_2^2$, and $-e_3^2$ using Equations (22)–(24). So far, the initial coaxial structure has been solved. It should be noted that for the single imaging system, f' takes a negative value, whereas for the secondary imaging system with an intermediate image plane, f' takes a positive value. However, in Zemax, the sign of the focal length is exactly the opposite; therefore, care must be taken to control the sign of the focal length during optimization.

In this paper, the initial structure of the coaxial three-mirror system is determined based on the mirror spacing. The system adopts a three-mirror structure without an intermediate image plane and with the aperture stop located at the secondary mirror. The distance from the primary mirror to the secondary mirror is equal to that from the secondary mirror to the tertiary mirror. This not only simplifies the calculation but also allows the primary and tertiary mirrors to be integrated and manufactured on a single piece of mirror material, thereby realizing the monolithic integration of the primary and tertiary mirrors and facilitating the assembly of the optical system.

Taking $d_1 = -90$, $d_2 = 90$ and $d_3 = -112$, the radius of curvature and conic constants for each surface can be obtained. The 3D structure diagram of the coaxial three-mirror system is shown in Figure 4, and the corresponding structural parameters are listed in Table 2.

Table 2. Parameters of the Coaxial Three-Mirror Optical Structure.

	Surf	Radius	Thickness	Glass	Conic
1	OBJ	Infinity	Infinity	—	—
2	Primary Mirror	−561.771	−90	MIRROR	−4.165
3	Secondary Mirror	−107.855	90	MIRROR	2.497
4	Third Mirror	−133.482	−112	MIRROR	0.190
5	IMA	Infinity	—	—	—

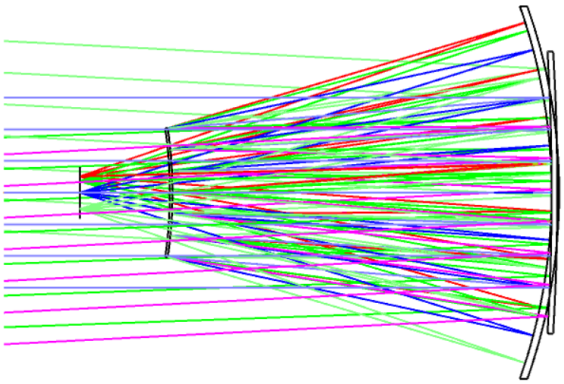


Figure 4. Schematic of the coaxial three-mirror system.

Based on the Seidel data in Table 3, spherical aberration, coma, astigmatism, and field curvature are all zero.

Table 3. Data of the First Four Seidel Aberrations for the Coaxial Three-Mirror Optical Structure.

Surface	SPHA S1	COMA S2	ASTI S3	FCUR S4
1	−0.000000	−0.000000	−0.000000	−0.000000
2	−0.009151	−0.000938	0.006117	−0.004722
Aperture Stop	−0.234066	−0.020136	−0.024592	0.024592
4	0.243217	0.021074	0.018475	−0.019871
Image Surface	0.000000	0.000000	0.000000	0.000000
Accumulated data	0.000000	0.000000	0.000000	0.000000

3.2. Off-Axis Design

To avoid the central obscuration inherent in coaxial systems, which leads to low light utilization, three ways of off-axis design are usually used for the system: field off-axis, aperture off-axis, or a combined field and aperture off-axis. In this paper, we adopt the combined field and aperture off-axis method for design, which not only avoids obscuration of the central rays but also introduces an inclination in the incident light, effectively simulating the operational state of a tilted camera.

Since operating off-axis can drastically increase optical aberrations, it is necessary to maintain a minimum separation of 10 mm between rays. This constraint prevents the system from reverting toward a coaxial configuration during optimization, which would cause ray vignetting, and ensures feasibility for manufacturing and assembly.

The implementation strategy involves ensuring that the distance d_1 from point A to the ray line BC exceeds 10 mm. That is, the distance from point A to BC. The equation of line BC can be expressed as $y = kx + b$, and the coordinates of point A are (X_A, Y_A).

By substituting X_A into the equation $y = kx + b$, the coordinates (X_A, Y'_A) of point A' are obtained. Subsequently, subtracting Y'_A from Y_A to make the result greater than a positive number. Implementing this strategy in optical design software and subsequently optimizing the system yields the results shown in Figure 5.

3.3. Introduction and Optimization Design of Freeform Surface

Following the obtaining of an unobscured off-axis three-mirror system, the tertiary mirror is characterized as a freeform surface to further correct off-axis aberrations and achieve a constant ground resolution design.

3.3.1. Selection of Freeform Surface Types

Since the optical system is symmetric about the YOZ plane, only the even-order terms of X in the XY polynomial are adopted. Considering various factors such as design performance, optimization speed, and manufacturability, a 4th-order XY polynomial is utilized to optimize the optical system. The surface expression is

$$z(x,y) = \frac{c\left(x^2+y^2\right)}{1+\sqrt{1-(1+k)c^2(x^2+y^2)}} + \sum_{i=1}^{N} A_i x^m y^n \quad (32)$$

In the above expression, the first term is the aspheric surface type term, (x, y, z) is the coordinates of the characteristic data points on the unknown surface, c is the curvature at the vertex of the fitted surface, k is the conic constant (quadratic coefficient), $\sum_{i=1}^{N} A_i x^m y^n$ is the term of the XY polynomial freeform surface, and A_i is the coefficient of the corresponding term.

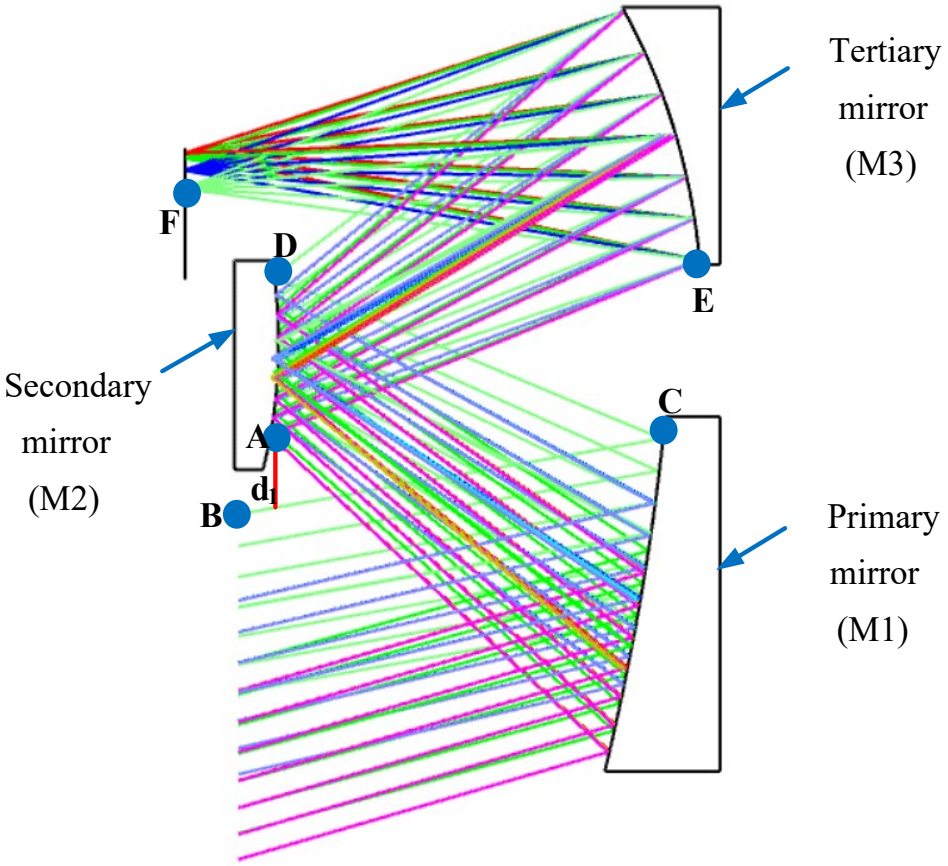


Figure 5. Schematic of ray-overlap prevention.

3.3.2. Introduction Sequence of Freeform Surfaces

In this design, the introduction of freeform surfaces follows the principle of gradual complexity: "coaxial before off-axis, and aspheric before freeform." The specific sequence is as follows:

(1) Construction of the coaxial initial structure

Based on the aberration theory, the initial coaxial three-mirror structure is solved. This structure is free of spherical aberration, coma, and astigmatism, serving as the foundation for subsequent design.

(2) Off-axis design

A combination of field off-axis and aperture off-axis is adopted to avoid central obscuration, and the spacings between mirrors are controlled to ensure a marginal ray separation greater than 10 mm. At this stage, the tertiary mirror remains a conic aspherical surface, and the image quality of the system is restored after preliminary optimization.

(3) Freeform surface replacement

The third mirror is replaced with an XY polynomial freeform surface, starting the optimization with initial coefficients set to 0, that is, the optimization starts with the original aspherical surface as the baseline.

(4) Ideal image point constraint based on FFL

According to the relationship between FFL and ground resolution, the desired FFL distribution is calculated. The ideal image point coordinates for each field of view are then derived using Equation (8). During optimization, the deviation between the actual image height and the ideal image height is added to the merit function as a constraint.

3.3.3. Optimize the Iteration Process

The optimization of the freeform surface employs a strategy of gradually increasing the polynomial order. The specific iteration process is as follows:

(1) Low-order optimization phase

Enable the low-order terms of the XY polynomial to correct the asymmetric aberrations introduced by the off-axis configuration. The merit function is primarily controlled by the deviation between actual image height and ideal image height, while maintaining structural constraints. The optimization goal is to make the image height at each field of view approach the expected value.

(2) High-order optimization phase

When the low-order optimization result tends to stabilize, the polynomial order is gradually increased to further correct residual aberrations. At this stage, appropriately increase the weight of the constraint on the ideal image points, and introduce MTF operands to constrain each field of view at the Nyquist frequency.

(3) Fine optimization phase

After the order of the freeform surface is determined, perform global optimization to balance image height accuracy, image quality, and structural constraints. Meanwhile, monitor the surface smoothness to avoid inflection points. Optimize the iteration until the image height of all fields meets the design requirements and the MTF curves approach the diffraction limit.

(4) Verification and adjustment phase

After the optimization, verify whether the actual FFL distribution matches the desired curve. If local deviations are significant, fine-tuning by increasing sampling points or adjusting local weights for the affected fields. Through the above phased optimization, the final off-axis three-mirror freeform surface system achieves highly uniform ground resolution across the full field of view and excellent image quality.

3.4. Image Quality Evaluation of the Off-Axis Three-Mirror System

The structural parameters, freeform surface coefficients, and structural schematic diagram of the final designed off-axis three-mirror optical system are shown in Table 4, Table 5, and Figure 6, respectively.

Table 4. Parameters of the Off-axis Three-Mirror Structure.

	Surf	Radius	Thickness	Glass	Conic
1	OBJ	Infinity	Infinity	—	—
2	Primary Mirror	−197.791	−50	MIRROR	−1.373
3	Secondary Mirror	−54.544	50	MIRROR	1.692
4	Third Mirror	−64.187	−50.919	MIRROR	−0.056
5	IMA	Infinity	—	—	—

Table 5. Third Mirror XY Polynomial Surface Coefficients.

Polynomial	Third Mirror Coefficients
y_1	-0.297
x_2	3.54×10^{-3}
y_2	3.141×10^{-3}
x_2y_1	-9.598×10^{-6}
y_3	-1.081×10^{-5}
x_4	-1.734×10^{-7}
x_2y_2	-3.9×10^{-7}
y_4	-2.227×10^{-7}
x_4y_1	-5.055×10^{-10}
x_2y_3	-1.215×10^{-9}
y_5	-7.49×10^{-10}

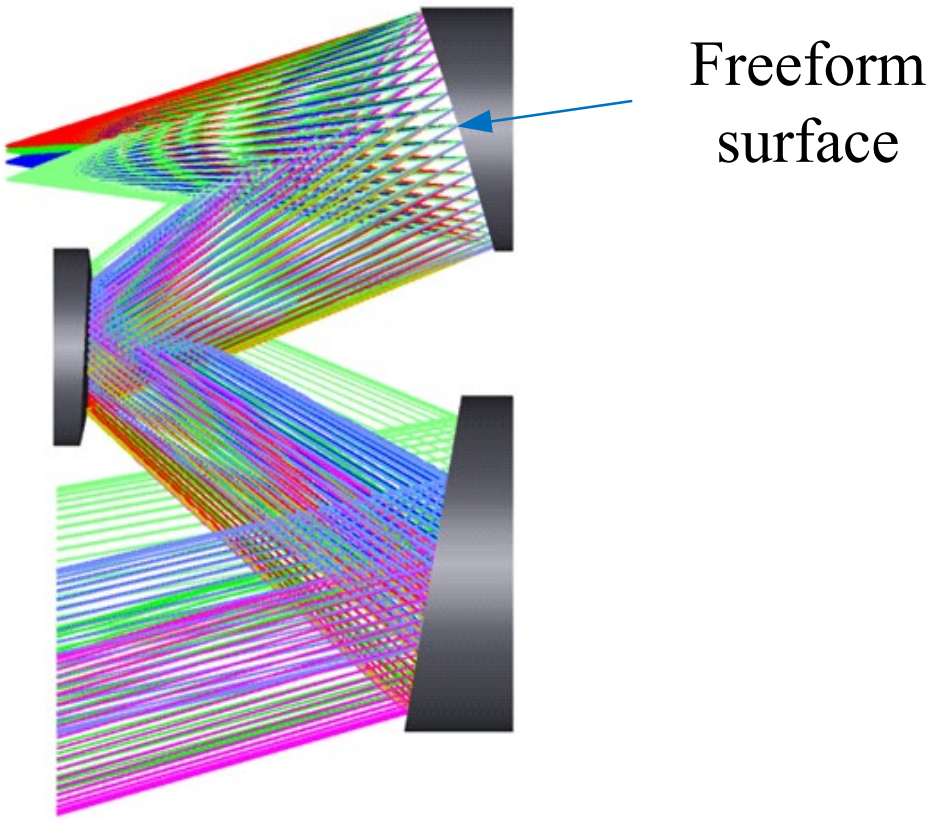


Figure 6. Schematic of the off-axis three-mirror optical system.

The MTF curves are shown in Figure 7, where the MTF values across all fields of view are close to the diffraction limit. The spot diagrams are shown in Figure 8, where the spot radius is smaller than the Airy disk.

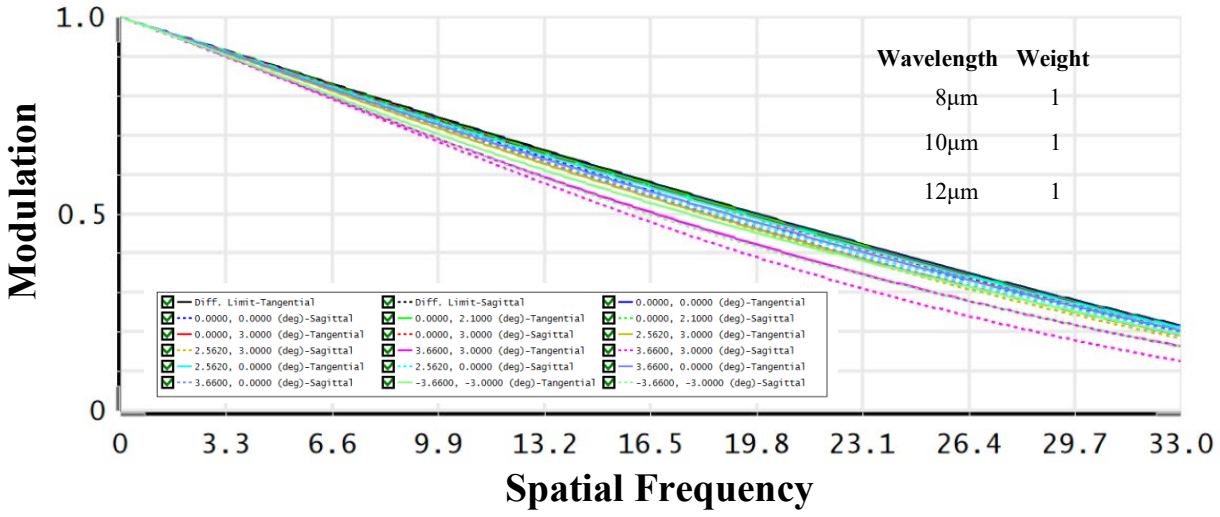


Figure 7. MTF of the off-axis three-mirror system.

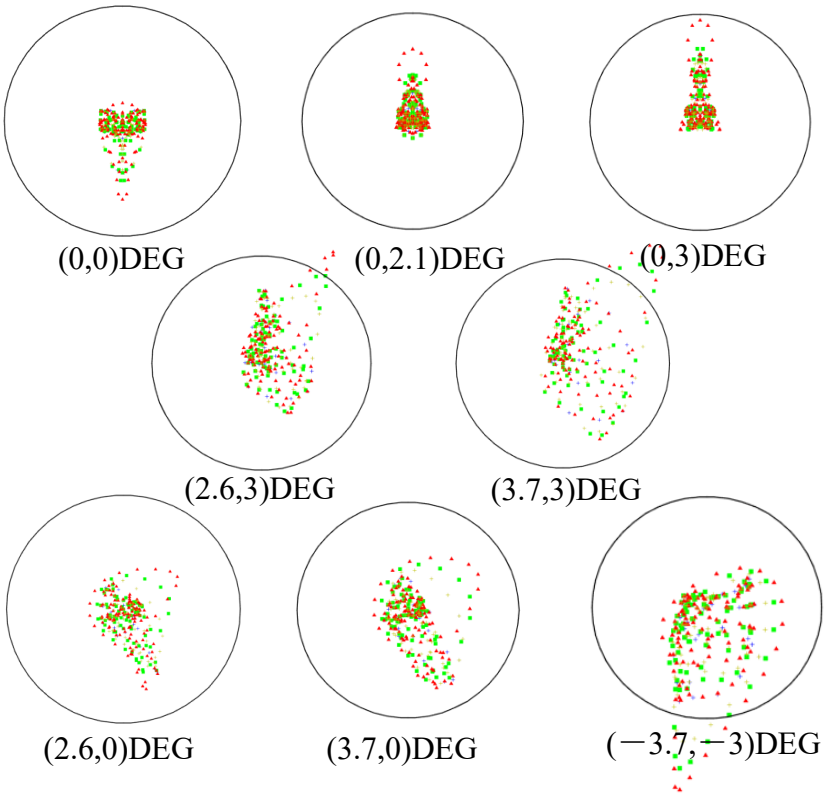


Figure 8. Spot diagrams of the off-axis three-mirror system.

3.5. Comparison of the Impact of Two Operating Modes on GSD

When the off-axis reflection system operates as a tilted camera, as shown in Figure 9a, in operation mode 1, the system observes point *B* with a 10° field of view and point *A* with a 16° field of view. The camera altitude is 2.5 km, and the detector pixel size is 15 μm. In operation mode 2, as shown in Figure 9b, the system observes point *A* with a 10° field of view and point *B* with a 16° field of view. The specific schematic diagram is shown in Figure 9.

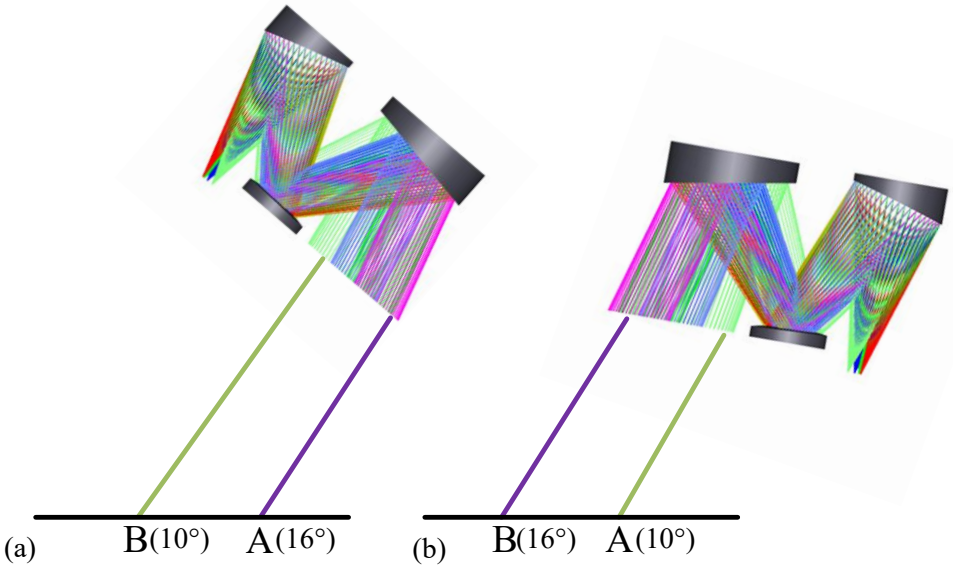


Figure 9. (**a**) Observation of point A at 16°; (**b**) Observation of point B at 16°.

According to Equation (7), the ground resolution GR at the sampling field of view was calculated and plotted as the green curve in Figure 10. As shown in Figure 9a, the 10° field of view is used to observe section *B*, and the 16° field of view is used for section *A*. Based on Equation (7), the GR at the sampling field of view is presented as the blue curve in Figure 10, whose variation range is significantly smaller than that of the second operation mode. In operation mode 1, the difference between the maximum and minimum GSD is 0.004, whereas in operation mode 2, the difference is 0.011.

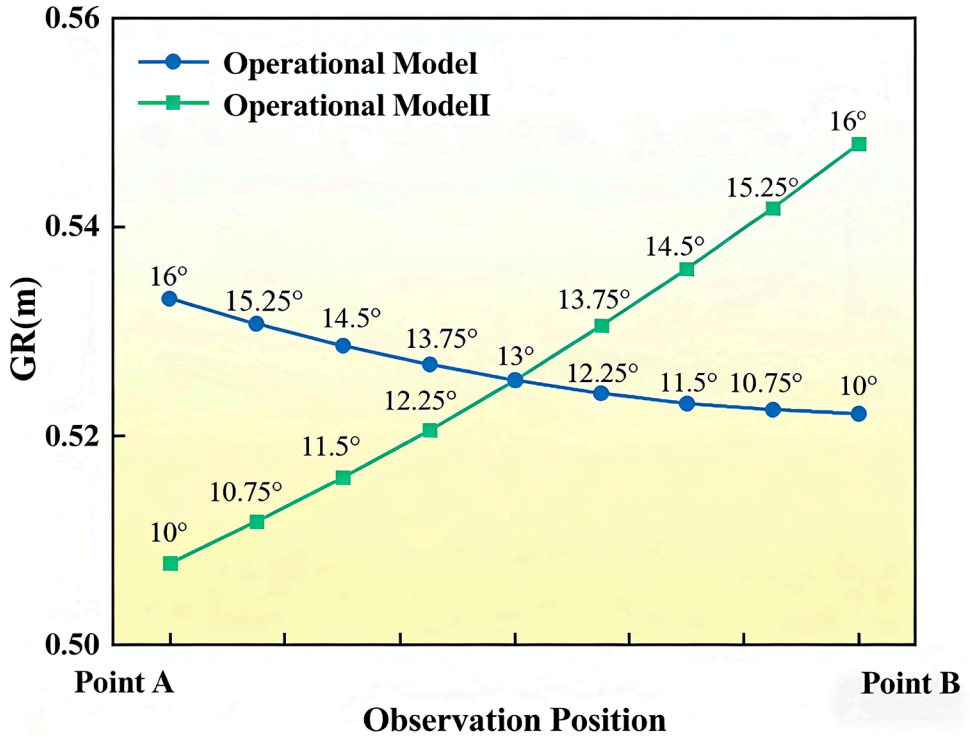


Figure 10. Ground resolution of two operating modes within the field of view range of 10°~16°.

4. Design and Image Quality Analysis of the Relay Zoom System

4.1. Design of the Relay System

This system adopts a two-stage imaging structure, consisting of a front off-axis three-mirror optical system as the primary objective, followed by a rear relay zoom lens group to form a complete imaging chain. The advantages of this structure are that it can realize pupil matching and image telecentricity, which is conducive to the implementation of subsequent zoom functionality.

As shown in Figure 11, the two-stage imaging optical system consists of primary optical systems M_1, M_2, and M_3 and relay systems G_1 and G_2. Chief rays from the marginal field of view enter the primary system at an incident angle θ, forming an intermediate image at plane A′B′, which is subsequently relayed by the relay optics to the secondary image plane A″B″. The aperture stop of the system is located on the secondary mirror M_2, which is imaged to position S′ by the front relay lens G_1 and then reimaged by the rear relay lens G_2, ultimately achieving image-side telecentric imaging.

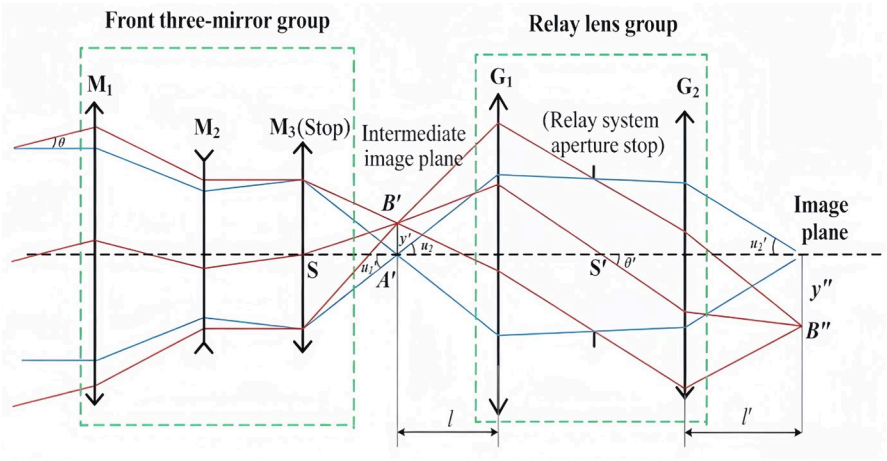


Figure 11. Schematic of the catadioptric two-stage imaging system.

Compared with the primary imaging system, the two-stage imaging optical system exhibits superior structural symmetry. The relay system is symmetric with respect to the intermediate image of the aperture stop, which enables high capability for off-axis aberration correction. This design is beneficial for reducing optical system distortion and improving irradiance uniformity across the image plane.

To achieve effective coupling between the primary optical system and the relay system, the following pupil matching relationship must be satisfied:

(1) Aperture matching: The position of the entrance pupil of the relay system should coincide with that of the exit pupil position of the primary optical system, and the size of the entrance pupil of the relay system needs to be greater than or equal to the size of the exit pupil of the primary optical system, to ensure that all the light collected by the primary optical system participates in imaging.

(2) F-number matching: The total F-number of the system is determined by the F-number of the relay system; that is, the image-side F-number of the primary optical system and the object-side F-number of the relay system should meet the transmission relationship.

(3) Image-space telecentric condition: To achieve image-space telecentricity, the intermediate image of the aperture stop should be located at the object-side focal point of the rear relay lens group, causing the chief rays to exit parallel to the optical axis.

The expression for the image height y″ in a two-stage imaging optical system is:

$$y'' = f_1' \cdot \beta_2 \cdot tan\theta \tag{33}$$

In this formula: f_1' is the focal length of the primary optical system; β_2 is the lateral magnification of the relay system.

The relay transmission system is divided into front and rear groups by the intermediate image of the aperture stop, and the apertures of the front and rear relay lenses satisfy the following conditions:

$$h_1' = l \times tanu_3', h_2' = l' \times tanu' \tag{34}$$

In this formula: h_1' is the aperture of the front lens group; h_2' is the aperture of the rear lens group.

The aperture of the relay lens is related to the F-number of the optical system and the distance from the relay lens to the intermediate image plane. To reduce the aperture of the relay lens, the relay lens should be placed as close as possible to the intermediate image plane. Therefore, by reducing the focal length of the relay lens to shorten the distance between the relay lens and the intermediate image plane, the aperture of the relay lens can be reduced.

4.2. Principle of the Zoom System

The above two-stage imaging structure provides the fundamental framework for achieving the zoom function in this design. Based on this framework, this paper designs the relay system as a mechanically compensated continuous zoom structure, and its zoom principle is as follows.

While maintaining a fixed image plane position, the continuous zoom optical system achieves zooming by moving two or more lens groups, enabling continuous clear imaging within the focal length range [17,18]. Continuous zoom optical systems follow the principle of object-image exchange and generally adopt a mechanical compensation structure, often utilizing a cam mechanism to realize zooming. During the zooming process, the cam drives the zoom group and the compensation group to move relative to each other along the optical axis, altering the interval between the zoom group and the compensation group to maintain image plane stability [19]. The schematic diagram of the optical system is shown in Figure 12.

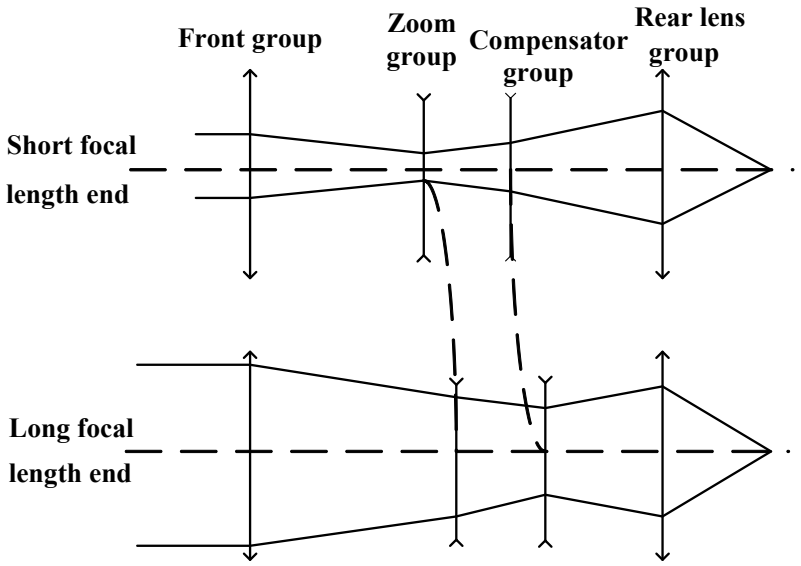


Figure 12. Schematic diagram of the zoom system.

When the zoom group moves by dq_2, the image plane displacement of the zoom group is $\left(1-\beta_2^2\right)dq_2$. The compensation group changes by dq_3, causing an image plane displacement of $\left(1-\beta_3^2\right)dq_3$. To maintain a fixed image plane position, the sum of the conjugate distance variations in the zoom group and compensation group must be zero; that is, the zoom system must satisfy the following condition:

$$\left(1-\beta_2^2\right)dq_2+\left(1-\beta_3^2\right)dq_3=0 \tag{35}$$

In Equation (35), β_2 and β_3 are the magnifications of the zoom group and compensation group during the zooming process, respectively, and dq_2 and dq_3 are the infinitesimal increments of the zoom group and compensation group. Their relationships with β_2 and β_3 are as follows:

$$\begin{cases} dq_2=\frac{f_{2'}}{\beta_2^2}d\beta_2 \\ dq_3=f_{3'}d\beta_3 \end{cases} \tag{36}$$

In Equation (36), f_2' and f_3' is the focal length of the zoom group and compensation group, respectively.

Substituting Equation (36) into Equation (35) yields the differential equation of the zoom system as follows:

$$\frac{1-\beta_2^2}{\beta_2^2}f_{2'}d\beta_2+\frac{1-\beta_3^2}{\beta_3^2}f_{3'}d\beta_3=0 \tag{37}$$

Assume that $U(\beta_2,\beta_3)$ is the primitive function, then we have

$$dU(\beta_2,\beta_3)=0 \tag{38}$$

Its general solution is

$$U(\beta_2,\beta_3)=f_{2'}\left(\frac{1}{\beta_2}+\beta_2\right)+f_{3'}\left(\frac{1}{\beta_3}+\beta_3\right)=C \tag{39}$$

In Equation (39), C is an undetermined constant.

Assuming that both the zoom group and compensation group are initially positioned at the short-focus end of the system, then

$$\beta_2=\beta_{2s};\ \beta_3=\beta_{3s} \tag{40}$$

In Equation (40), β_{2s} and β_{3s} are the magnifications of the zoom group and compensation group, when the system is at the short-focus end.

Substituting Equation (39) into Equation (40) yields:

$$f_{2'}\left(\frac{1}{\beta_{2s}}+\beta_{2s}\right)+f_{3'}\left(\frac{1}{\beta_{3s}}+\beta_{3s}\right)=C \tag{41}$$

To eliminate the undetermined constant C, subtract Equation (41) from Equation (39) to obtain:

$$f_{2'}\left(\frac{1}{\beta_2}-\frac{1}{\beta_{2s}}+\beta_2-\beta_{2s}\right)+f_{3'}\left(\frac{1}{\beta_3}-\frac{1}{\beta_{3s}}+\beta_3-\beta_{3s}\right)=0 \tag{42}$$

When balancing aberrations in a continuous zoom optical system, the approach is fundamentally consistent with that of a fixed-focus optical system. Both require correcting primary aberrations as much as possible and minimizing higher-order aberrations to achieve good image quality across the full field of view and full aperture. Additionally, a continuous zoom optical system must ensure image quality at every focal length position.

Consequently, continuous zoom optical systems have stricter requirements for aberration correction and present greater design challenges.

4.3. Design and Image Quality Analysis of the Zoom System

After completing the design of the front-end reflective system, two methods can be adopted to achieve zoom capability: zooming via the movement of three mirrors or zooming via a refractive zoom lens group placed after an off-axis reflective system. The disadvantage of mirror-based zooming is that the assembly process is excessively difficult, while refractive zooming offers advantages in ease of assembly and superior image quality.

The core advantage of incorporating a relay lens group and achieving zooming through movement within this group lies in its ability to provide flexible focal length adjustment while maintaining the overall stability of the system. Since the relay group inherently functions to relay the image plane and transmit the optical path, moving the zoom elements internally ensures that the image plane position remains fixed. This eliminates the need for additional mechanical compensation, thereby significantly simplifying the focusing process and enhancing operational efficiency.

The zoom diagram of the relay lens group is shown in Figure 13. Zooming is achieved by moving the relay lens group, wherein the first lens from right to left is the fixed group, the second and third lenses form the variable zoom group, the fourth lens is the compensation group, and the fifth and sixth lenses constitute the rear fixed group.

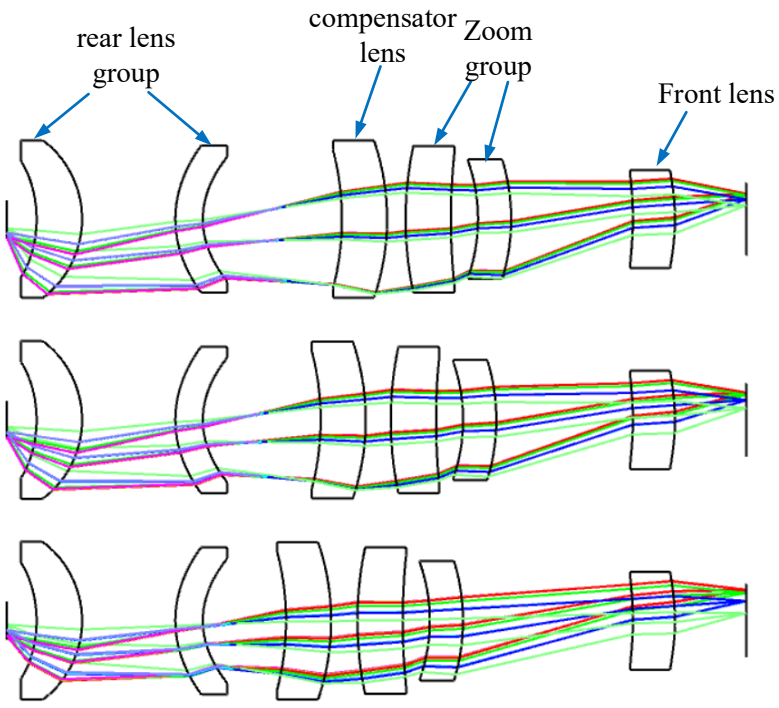


Figure 13. Zoom layout of relay lens group.

Meanwhile, the detailed structural parameters of the relay lens group are shown in Tables 6 and 7.

The current system design optimizes three characteristic positions: the short focus end, the medium focus end, and the long focus end. The lens zoom interval parameters corresponding to each position are shown in Table 8.

Table 6. Lens data for the zoom group.

Surface Number	Surface Type	Radius of Curvature r	Thickness d	Material
12	Standard	INFINITY	−35.673	
13	Apstandard	−101.916	−21.088	GERMANIUM
14	Apstandard	−141.603	Zoom Separation 1	
15	Standard	−101.160	−16.607	ZNSE
16	Apstandard	−87.153	−13.581	
17	Standard	313.360	−22.689	GERMANIUM
18	Standard	174.908	Zoom Separation 2	
19	Standard	−120.434	−22.619	GERMANIUM
20	Standard	−134.541	Zoom Separation 3	
21	Apstandard	39.689	−13.786	ZNSE
22	Apstandard	53.48	−46.733	
23	Apstandard	−48.277	−22.816	GERMANIUM
24	Apstandard	−59.436	−15.000	
Image plane	INFINITY			

Table 7. Aspheric coefficient.

Surface	Conic Constant	4th-Order	6th-Order	8th-Order
13	−10.195	5.60×10^{-10}	-2.39×10^{-7}	-3.41×10^{-13}
14	−34.046	7.65×10^{-10}	3.18×10^{-7}	5.91×10^{-13}
16	0.152	2.61×10^{-12}	-5.21×10^{-8}	-7.65×10^{-15}
21	−0.59	1.03×10^{-9}	-1.22×10^{-6}	-6.87×10^{-13}
22	−0.55	3.43×10^{-10}	-3.22×10^{-7}	-1.79×10^{-13}
23	0.077	1.31×10^{-10}	3.39×10^{-7}	-5.16×10^{-14}
24	−0.086	-1.11×10^{-9}	6.02×10^{-7}	-3.53×10^{-13}

Table 8. Lens zoom interval parameters.

Surface	Short Focus End	Medium Focus End	Long Focus End
Zoom Separation 1	−85.197	−68.488	−61.041
Zoom Separation 2	−13.188	−12.539	−9.311
Zoom Separation 3	−41.695	−59.053	−69.728

The data in the table shows that as the focal length changes from the short focus end to the long focus end, the zoom separation 1 (fixed group—zoom group) decreases from −85.197 mm to −61.041 mm, and the zoom separation 3 (compensator group—rear fixed group) increases from −41.695 mm to −69.728 mm. The zoom group and compensator group move according to a nonlinear law to maintain image plane stability. The zoom curve of the system is shown in Figure 14.

The two-dimensional schematic diagram of the system and the MTF charts at the short focus end, medium focus end, and long focus end are shown in Figure 15 and Figure 16, respectively.

To comprehensively evaluate the stability of the system's imaging quality during the continuous zooming process, in addition to the short focus end, medium focus end, and long focus end, two intermediate focal lengths of 62.5 mm and 87.5 mm are selected for image quality analysis.

Figure 17 shows the MTF curves of the system at the focal lengths of 62.5 mm and 87.5 mm, respectively. Combined with Figure 16, it can be seen that the system exhibits excellent imaging quality over the entire zoom range.

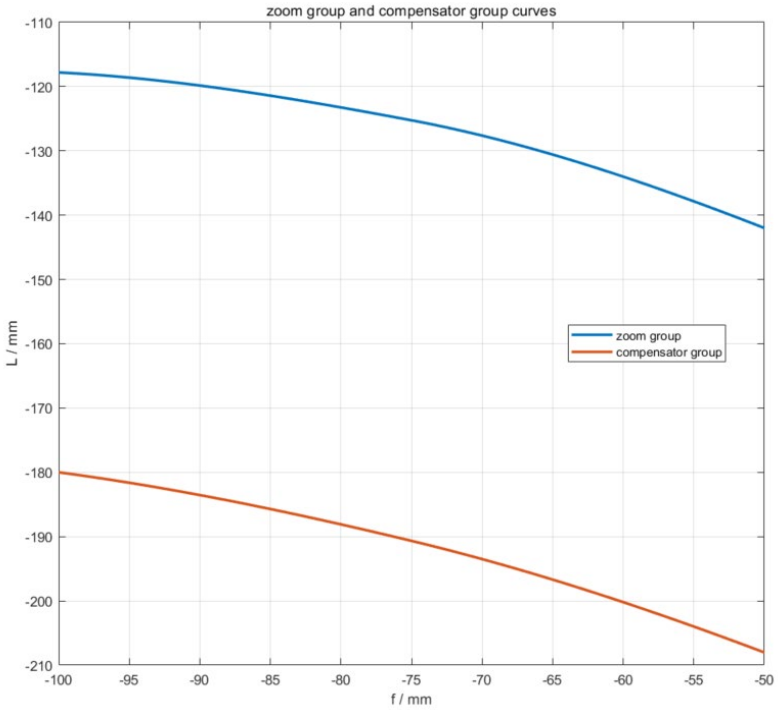


Figure 14. Zoom curve of the system.

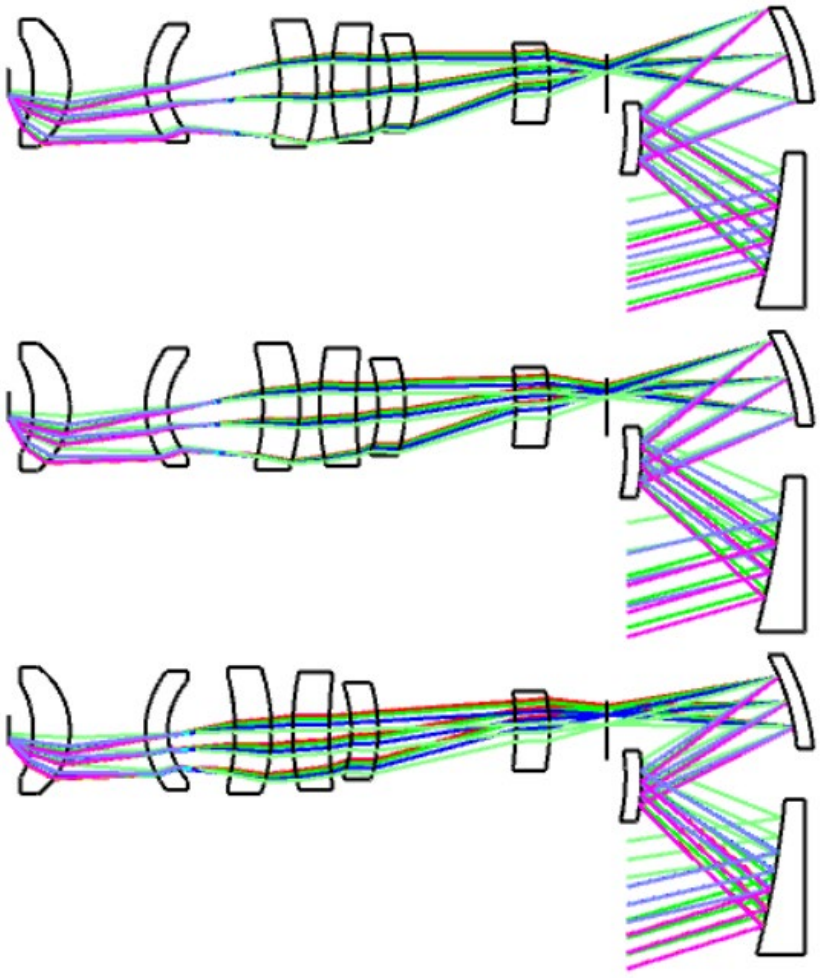
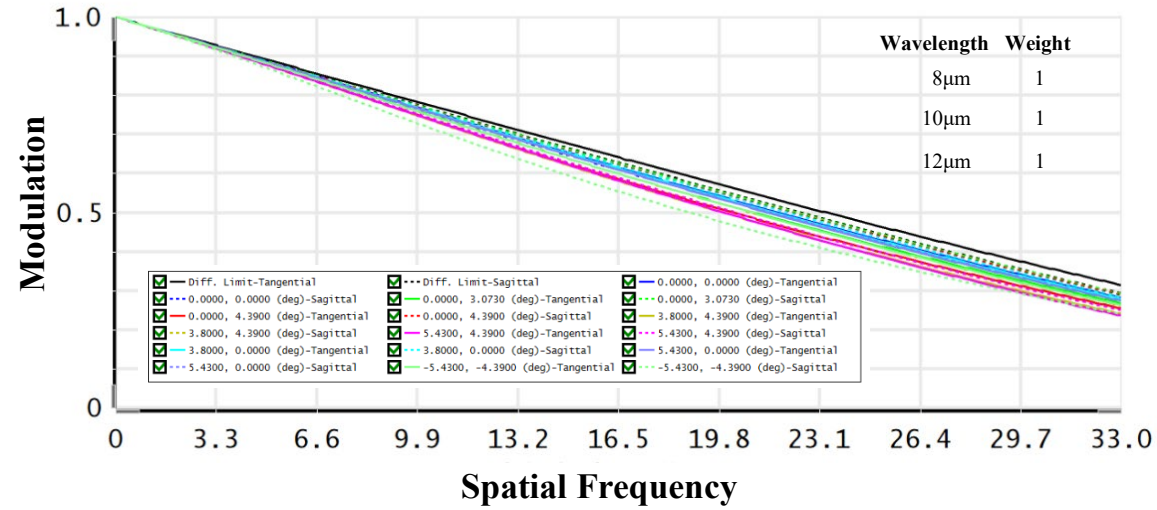
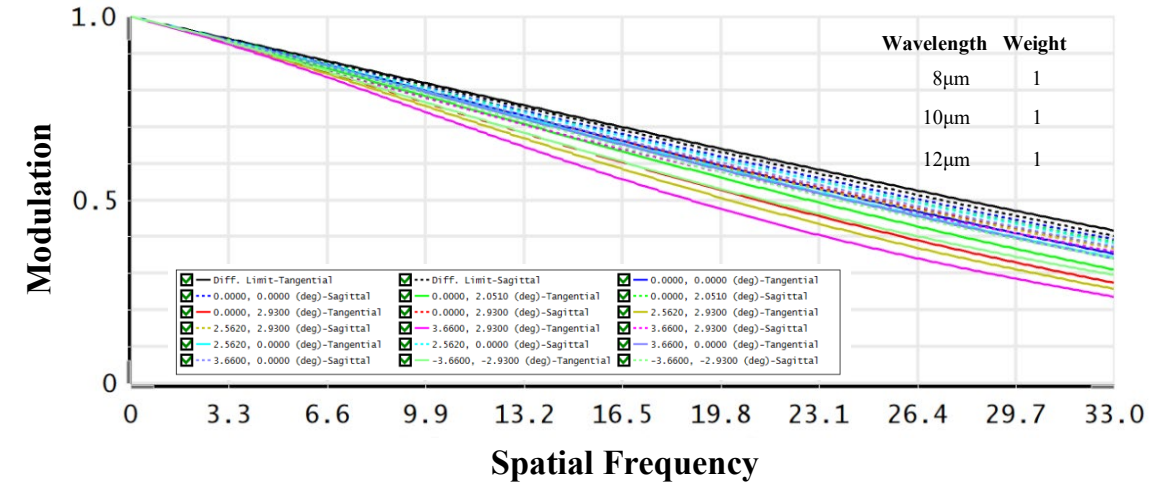


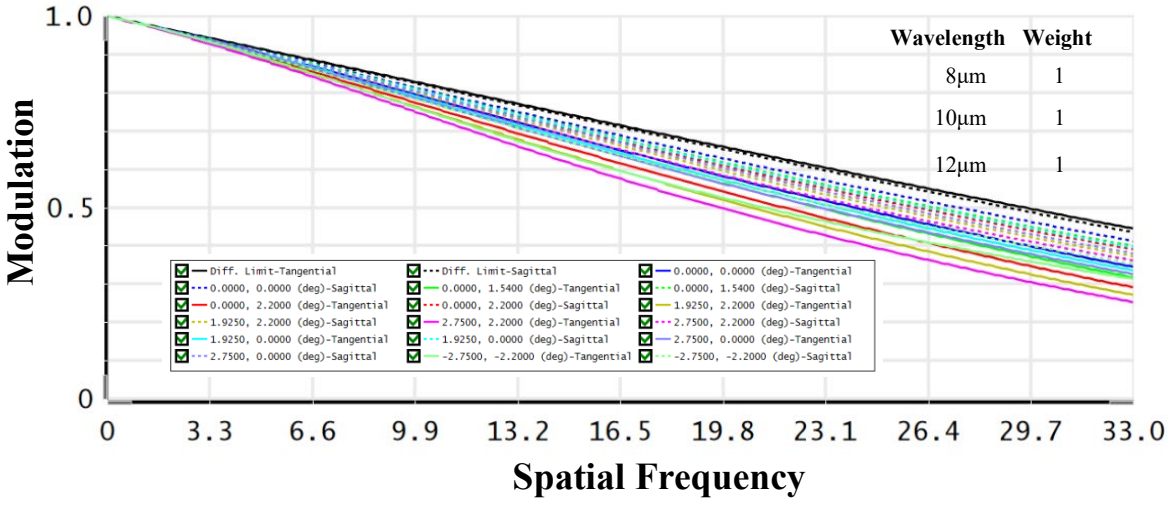
Figure 15. Two-dimensional layout of the system.



(**a**)



(**b**)



(**c**)

Figure 16. (**a**) MTF at the short focal end; (**b**) MTF at the medium focal end; (**c**) MTF at the long focal end.

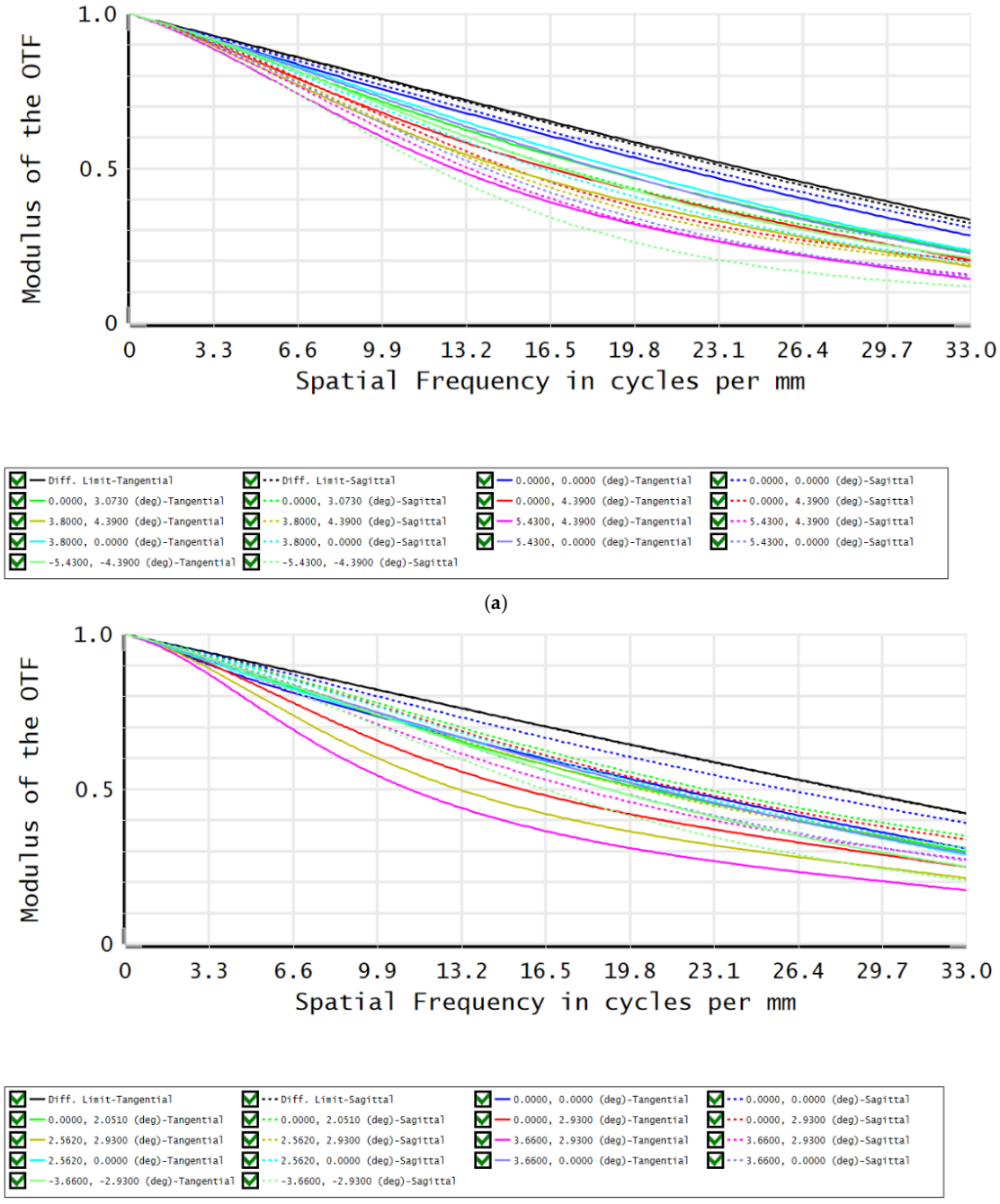


Figure 17. (**a**) MTF at 62.5 mm; (**b**) MTF at 87.5 mm.

By comparing the MTF curves at the five focal positions, it can be seen that with the change in focal length, the fluctuation range of the MTF value in each field of view is less than 0.05, with no obvious degradation or abrupt changes. The imaging quality of the system remains stable during the continuous zooming process, meeting the design requirements.

4.4. Athermalization Analysis of the System

LWIR optical systems are sensitive to temperature variations. Temperature fluctuations can alter the radius of curvature, thickness, and refractive index of optical elements, leading to image plane drift and degradation of imaging quality. To ensure the imaging stability of the system, an adiabatic analysis is carried out for the operating temperature range of −40 °C to +60 °C.

According to the actual operating conditions of the UAV airborne environment, three typical temperature points are selected for image quality evaluation: −40 °C low temperature, +20 °C normal temperature and +60 °C high temperature, corresponding to the short focus end, medium focus end, and long focus end positions, respectively.

Figure 18 shows the MTF curves of the system under three conditions: short focus end at −40 °C, medium focus end at +20 °C, and long focus end at +60 °C. It can be observed that the influence of temperature variation on the system imaging quality follows a regular pattern: the image quality is optimal at normal temperature and degrades slightly at both low and high temperatures. Specifically, the impact of high temperature on the long focus end is slightly more pronounced than the impact of low temperature on the short focus end, because the light rays at the long focus end undergo larger refraction angles, making the system more sensitive to temperature-induced refractive index changes. Furthermore, the MTF curves remain smooth at all three temperature points without obvious aberration mutations, indicating that the system has good thermal stability.

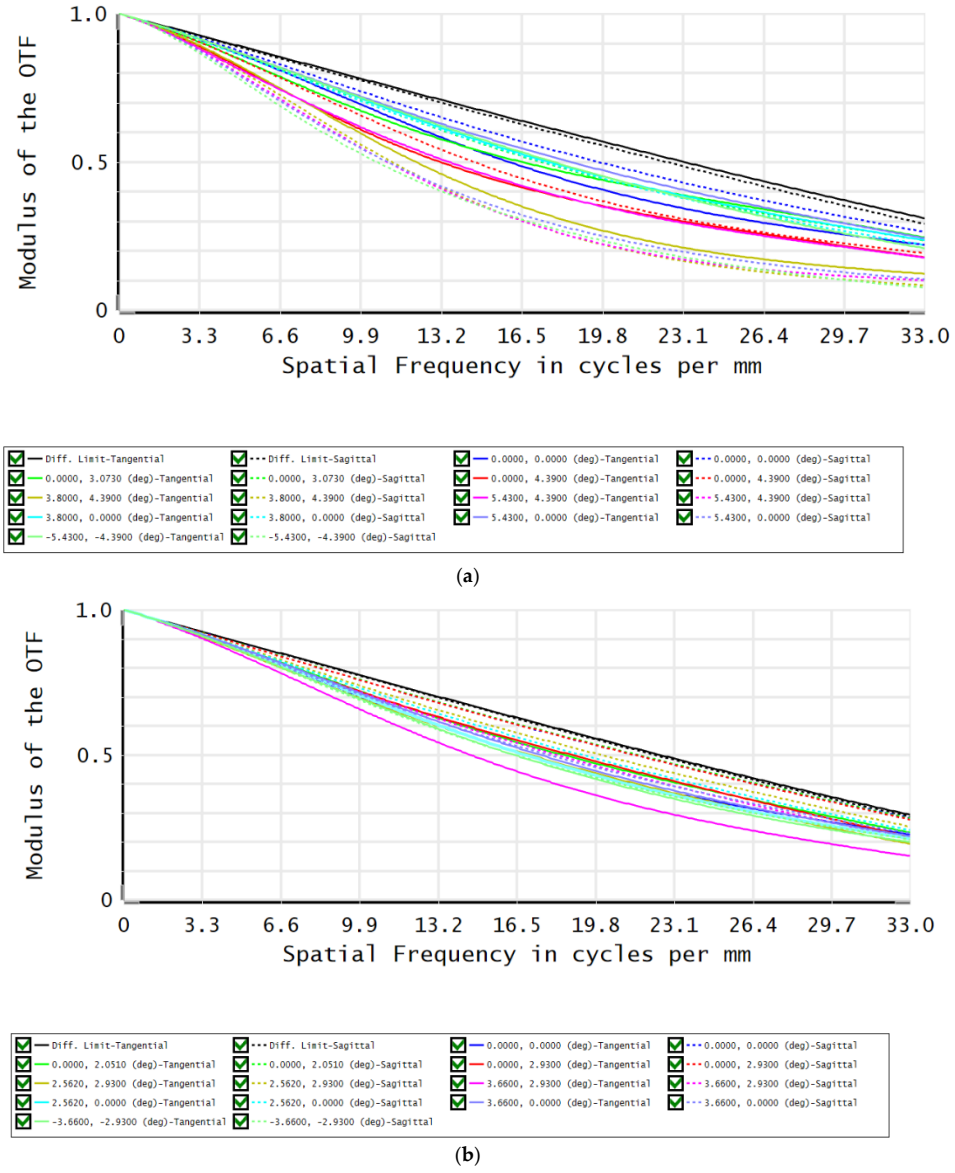
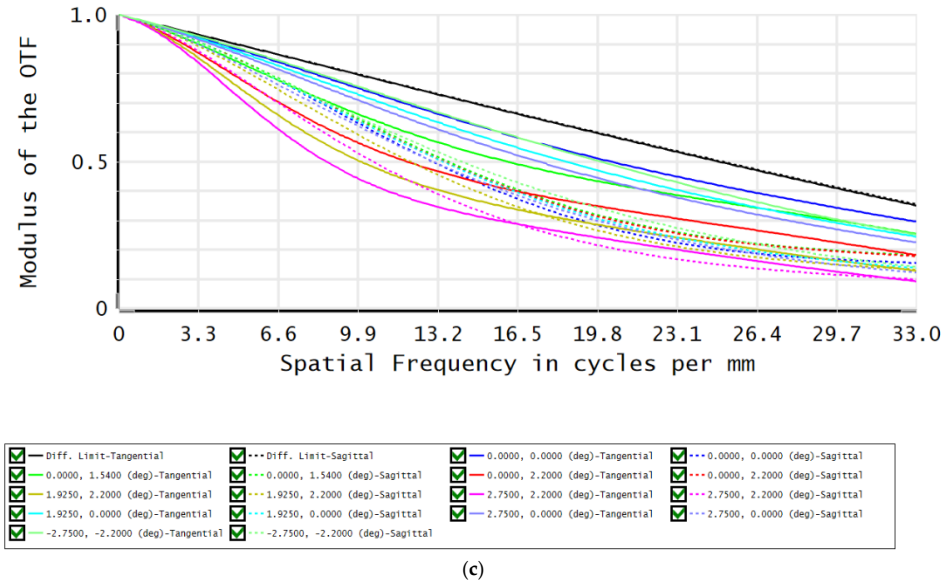


Figure 18. *Cont.*



(**c**)

Figure 18. (**a**) MTF at the short focus end at −40 °C; (**b**) MTF at the medium focus end at +20 °C; (**c**) MTF at the long focus end at +60 °C.

Meanwhile, we analyzed the chief ray angle (CRA). The results show that the CRA of the center field of view is 29.495° and that of the edge field of view is 35.697°. This range meets the matching requirements for the LWIR detector.

5. Optimization Result Analysis for Equal Ground Resolution

As shown in Figure 19, the black curve represents the desired FFL curve calculated using Equation (7), the blue curve represents the FFL curve before optimization, and the red curve represents the FFL curve after optimization. It can be seen from the figure that black and red curves show good agreement in the 10–14° range, while some deviation occurs at fields of view greater than 14°. This deviation is due to the limitations of the freeform surface polynomial order and optimization sampling points, which restrict aberration correction at the edge of the field of view. However, the impact of this deviation on the GR is controllable, and it still meets the design specifications.

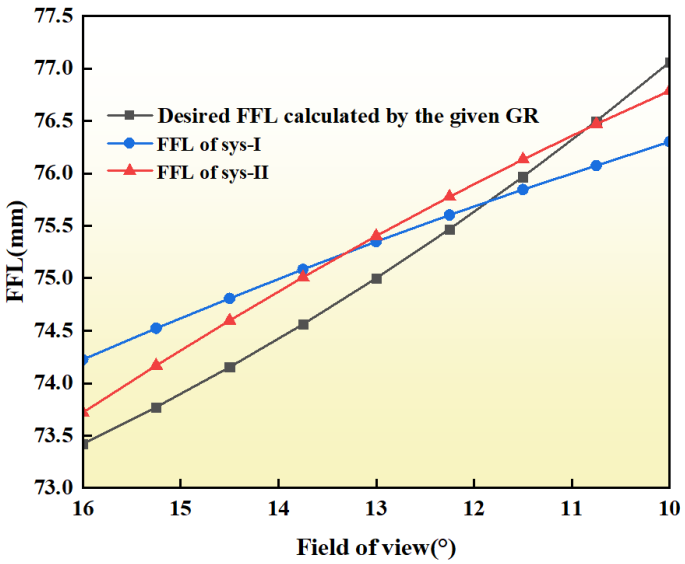


Figure 19. Comparison of three different field-of-view focal lengths.

As shown in Figure 20, the blue curve represents the system's GR before optimization, while the red curve represents the GR after optimization. By calculating the difference between the highest and lowest points of each curve, the comparison reveals that the GR of the red curve is more uniform. The maximum resolution difference before optimization was 0.011 m, which was reduced to 0.004 m through optimization.

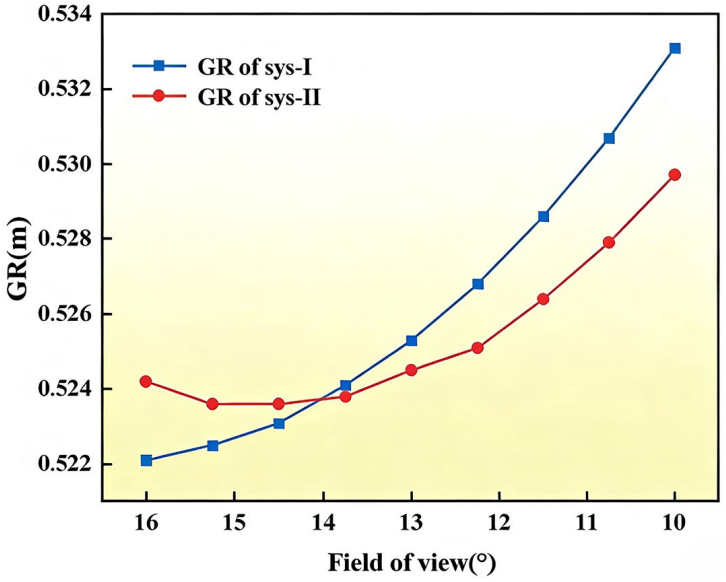


Figure 20. Comparison of the resolution before and after the system.

By controlling the FFL function during the design process, we achieved a tilted camera with an improved GR distribution. This not only demonstrates that FFL can be used to analyze the GR of tilted cameras but also improves GR uniformity in tilted cameras.

To further verify the performance advantages of this design in terms of constant ground resolution, the optimized ground resolution uniformity index is compared horizontally with the airborne oblique imaging systems reported in other literature. Table 9 presents the performance comparison between this system and existing constant ground resolution systems.

Table 9. Performance comparison with existing constant ground resolution systems.

Items for Comparison	MWIR Fixed Focus System	LWIR Zoom System
Operating waveband	3–5 μm	8–12 μm
Focal length type	60 mm fixed focal length	50–100 mm continuous zoom
Flight altitude	2 km	1.6–3.3 km
Detector pixel size	15 μm	15 μm
Maximum GR difference before optimization	0.019 m	0.011 m
Maximum GR difference before optimization	0.003 m	0.004 m

6. Conclusions

The long-wave infrared zooming optical system with constant ground resolution designed in this paper can achieve continuous zooming when the UAV flies at an altitude of 1.6 km to 3.3 km. In the front-end off-axis reflective system, free-form surfaces expressed by XY polynomials are employed to increase the degrees of design freedom. The results show that the system significantly reduces the deviation in the system's ground resolution across each field of view, meeting the constant ground resolution requirement. Subsequently, the relay lens group achieves the zoom function while correcting aberrations and reducing

the number of lens groups. The image quality is excellent, with the MTF approaching the diffraction limit and spot diagrams confined within the Airy disk.

Author Contributions: Conceptualization, Z.Y. and L.G.; methodology, B.W. and L.G.; software, W.Z. and B.W.; validation, Z.Y. and L.Y.; formal analysis, W.Z. and B.W.; investigation, Z.Y. and L.W.; resources, Z.Y., L.W. and L.Y.; data curation, W.Z.; writing—original draft preparation, Z.Y. and W.Z.; writing—review and editing, B.W. and Y.L.; visualization, W.Z. and B.W.; supervision, Z.Y. and L.Y.; project administration, Z.Y.; funding acquisition, Z.Y. and Y.L. All authors have read and agreed to the published version of the manuscript.

Funding: This research was funded by the Natural Science Basic Research Program of Shaanxi Province (No. 2025JC-YBMS-082) and the Natural Science Basic Research Program of Shaanxi Province (No. 2025JC-YBMS-744).

Institutional Review Board Statement: Not applicable.

Informed Consent Statement: Not applicable.

Data Availability Statement: Data underlying the results presented in this paper are not publicly available at this time, but may be obtained from the authors upon reasonable request.

Acknowledgments: The authors sincerely appreciate all financial and technical support.

Conflicts of Interest: The authors declare no conflicts of interest.

Abbreviations

The following abbreviations are used in this manuscript:

LWIR	Long-wave infrared
MWIR	Mid-wave infrared
GR	Ground resolution
UAV	Unmanned Aerial Vehicle
MTF	Modulation transfer function
FFL	Field-of-view focal length
CRA	Chief ray angle

References

1. Rolland, J.P.; Davies, M.A.; Suleski, T.J.; Evans, C.; Bauer, A.; Lambropoulos, J.C.; Falaggis, K. Freeform optics for imaging. *Optica* **2021**, *8*, 161–176. [CrossRef]
2. Bauer, A.; Takaki, N.; Rolland, J.P. Design methods for imaging with freeform optics. *Optica* **2025**, *12*, 1775–1793. [CrossRef]
3. Mikš, A.; Novák, J.; Novák, P. Method of zoom lens design. *Appl. Opt.* **2008**, *47*, 6088–6098. [CrossRef] [PubMed]
4. Stewart, W. Freeform Optics: Notes from the Revolution. *J. Opt. Photonics News* **2017**, *28*, 34.
5. Zhu, J.; Zhang, B.; Hou, W.; Bauer, A.; Rolland, J.P.; Jin, G. Design of an oblique camera based on a field-dependent parameter. *J. Appl. Opt.* **2019**, *58*, 5650–5655. [CrossRef] [PubMed]
6. Wu, W.; Jin, G.; Zhu, J. Optical design of the freeform reflective imaging system with wide rectangular FOV and low F-number. *J. Results Phys.* **2019**, *15*, 102688. [CrossRef]
7. Wu, W.; Zhang, B. Freeform imaging system with a resolution that varies with the field angle in two dimensions. *J. Opt. Express* **2021**, *29*, 37354–37367.
8. Wu, H.; Wang, W. Design of airborne miniaturized middle wavelength infrared continuous zoom optical system. *Infrared Technol.* **2021**, *43*, 1177–1182.
9. Cheng, Y.; Ouyang, Q.; Yao, C.; Liu, L.; Li, Z.; Hao, Q. Dielectric-elastomer-driven long-wave infrared Alvarez lenses for continuous zooming imaging. *Infrared Phys. Technol.* **2024**, *143*, 105614. [CrossRef]
10. Liu, H.; Xu, Z.; Wei, Y.; Han, K.; Peng, X. Multispectral non-line-of-sight imaging via deep fusion photography. *Sci. China* **2025**, *68*, 197–215. [CrossRef]
11. Yang, Z.; Gao, S.; Chen, Q.; Wu, B.; Xu, Q.; Gong, L.; Yang, L. Airborne Constant Ground Resolution Imaging Optical System Design. *Photonics* **2025**, *12*, 390. [CrossRef]

12. Meng, Q.; Wang, H.; Yan, Z. Residual aberration correction method of the three-mirror anastigmat (TMA) system with a real exit pupil using freeform surface. *J. Opt. Laser Technol.* **2018**, *106*, 100–106. [CrossRef]
13. Zhang, J.; Qin, T.; Xie, Z.; Sun, L.; Lin, Z.; Cao, T.; Zhang, C. Design of airborne large aperture infrared optical system based on monocentric lens. *Sensors* **2022**, *22*, 9907. [CrossRef] [PubMed]
14. Yan, J.; Sun, Q.; Liu, Y.; Zhou, H.; Huan, K.; Shi, X.G. High ratio long-wave infrared continuous zoom system. In *International Symposium on Photoelectronic Detection and Imaging 2013: Infrared Imaging and Applications*; SPIE: Bellingham, WA, USA, 2013; Volume 8907, pp. 216–224.
15. Chao, C.; Liao, Z.; Yu, B.; Xing, T. Design of large zoom ratio long-wave infrared zoom system with compound zoom method. *Opt. Eng.* **2018**, *57*, 025104. [CrossRef]
16. Luo, Y.; Li, L.; Feng, Y.; Zhao, H.; Li, X.; Bai, Q. Design method for initial structure of freeform surface optical system. *J. Acta Opt. Sin.* **2021**, *41*, 228–234.
17. Fuerschbach, K.; Rolland, J.P.; Thompson, K.P. Theory of aberration fields for general optical systems with freeform surfaces. *J. Opt. Express* **2014**, *22*, 26585–26606. [CrossRef] [PubMed]
18. Kevin, T. Description of the third-order optical aberrations of near-circular pupil optical systems without symmetry. *J. Opt. Soc. Am. A* **2005**, *22*, 1389–1401.
19. Thompson, K.P.; Rolland, J.P. Freeform optical surfaces: A revolution in imaging optical design. *J. Opt. Photonics News* **2012**, *23*, 30–35. [CrossRef]

Disclaimer/Publisher's Note: The statements, opinions and data contained in all publications are solely those of the individual author(s) and contributor(s) and not of MDPI and/or the editor(s). MDPI and/or the editor(s) disclaim responsibility for any injury to people or property resulting from any ideas, methods, instructions or products referred to in the content.